# Chapter 7

# Ultrasound Contrast Agent Microbubble Dynamics

Marlies Overvelde, Hendrik J. Vos, Nico de Jong, and Michel Versluis

**Abstract.** Ultrasound contrast agents are traditionally used in ultrasound-assisted organ perfusion imaging. Recently the use of coated microbubbles has been proposed for molecular imaging applications where the bubbles are covered with a layer of targeting ligands to bind specifically to their target cells. In this chapter we describe contrast agent microbubble behavior starting from the details of free bubble dynamics leading to a set of equations describing the dynamics of coated microbubbles. Experimentally, the dynamics of ultrasound contrast agent microbubbles is temporally resolved using the ultra-high speed camera Brandaris 128. The influence of a neighboring wall is investigated by combining the Brandaris camera with optical tweezers. It was observed that the presence of the wall can alter the bubble response. A detailed description of the bubble-wall interaction may therefore lead to improved molecular imaging strategies.

## 7.1 Introduction

Ultrasound is widely used in medical imaging in gynecology, cardiology, radiology and urology. In cardiology for example ultrasound imaging is used to assess the heart wall motion and the heart valves. Ultrasound Contrast Agents [22] (UCA) are used to enhance endocardial border delineation and to assess perfusion. UCAs consist of small microbubbles with a radius of 1 to 5 μm. The bubbles have a high scattering cross section because of their compressibility giving rise to a strong echo. The microbubbles are coated with a phospholipid monolayer, a polymeric shell or proteins to reduce the capillary pressure and to prevent them from dissolving in the blood, see Figure 7.1.

An emerging application is the use of these type of microbubbles in molecular imaging. Here the bubbles contain targeting ligands which bind specifically to their target cells, for diagnosis at a cellular level. For such molecular imaging applications it is desirable to distinguish freely floating microbubbles from targeted ones.

While the response of a bubble depends on the applied acoustic pressure, it also depends strongly on the applied ultrasound frequency. At low acoustic

Paradossi, G., Pellegretti, P., Trucco, A. (Eds.)
Ultrasound contrast agents. Targeting and processing methods for theranostics

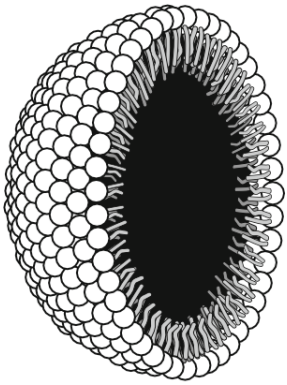

**Fig. 7.1.** Schematic drawing of a microbubble with a phospholipid monolayer

driving the bubble response is maximum at its resonance frequency. The resonance frequency of microbubbles with a radius of 1–5 μm is in the megahertz range, which nicely (and for obvious reasons) coincides with the optimum imaging frequencies used in medical ultrasound imaging. For higher acoustic pressures the microbubbles show strong non-linear behavior, producing higher harmonics. Most contrast-enhanced ultrasound imaging techniques, such as power modulation [3] and pulse inversion [19], exploit the second harmonic signal to distinguish tissue from contrast.

A targeted microbubble is a complex system containing a gas core, a shell and targeting ligands. To understand the behavior of these targeted microbubbles we need to understand the dynamics of a gas bubble and the influence of its shell and targeting ligands. There exists a full theoretical and experimental understanding of the behavior of uncoated gas bubbles in the mm-range in free space [15, 17, 21, 24, 30, 31, 33, 35] and some of these models are also used to describe the bubble behavior in the μm-range. The validation of these models in the μm-range has been limited because of experimental complexity, predominantly because of the rather short lifetime of the uncoated bubbles. Several theoretical models have been developed for bubbles with a viscoelastic coating [6, 7, 18, 36]. Recently, these models were extended to account also for buckling and rupture of the shell [26]. Acoustical characterization of bubble suspensions and acoustical and optical experiments for example with the Brandaris 128 camera [5], see Figure 7.2, performed on single bubbles confirm the physical picture governed by the visco-elastic properties of the shell [16,26,38]. The change in dynamics between untargeted and targeted microbubbles has been investigated by Zhao et al. [40, 41] and Lankford et al. [23].

In general, experiments on single UCA microbubbles are performed on bubbles floating against a (capillary) wall. This may not represent the ideal comparison to theory and numerical simulations, as in the models the bubble is assumed to reside in an infinite medium. Garbin at al. [14] used an optical tweezers setup to manipulate single UCA microbubbles and it was shown

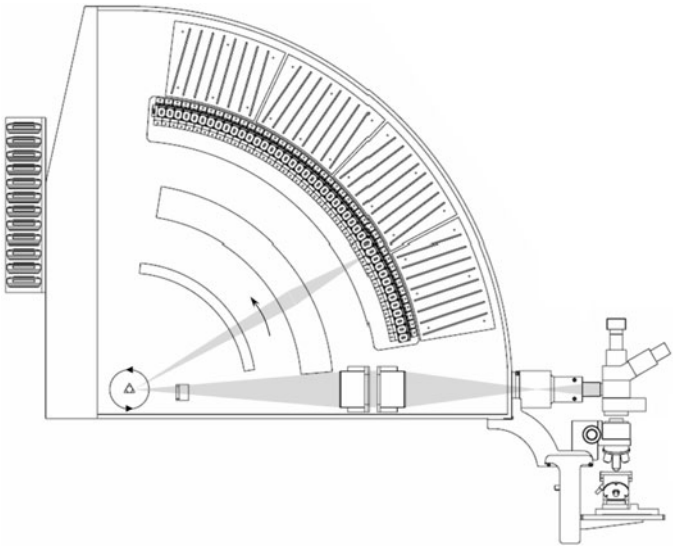

**Fig. 7.2.** Schematic drawing of the Brandaris 128 camera. The rotating mirror sweeps the light beam projecting the microscope image on the CCD's. The mirror sweeps the image over the CCD's with a minimum interframe time of 40 ns or equivalent a framerate of 25 Mfps

experimentally that the UCA microbubbles' dynamics is hampered by the presence of a wall. A theory on the influence of a rigid wall exists for uncoated gas bubbles and it includes translational oscillations [9, 27]. The influence of the wall on the bubble response may prove to be useful for the discrimination of targeted and freely floating microbubbles in molecular imaging applications.

In the following sections the current understanding of the dynamics of single UCA microbubbles, both theoretically and experimentally, is discussed. Section 7.2 starts with a description of the behavior of an uncoated bubble using the non-linear Rayleigh-Plesset equation. Through linearization we derive an expression for the resonance curve, the resonance frequency and the damping. In section 7.3 we describe in more detail the influence of a viscoelastic shell, while the influence of a rigid wall on the dynamics of microbubbles is discussed in section 7.4. The chapter is concluded with a discussion and conclusion in section 7.5.

## 7.2 Dynamics of a free gas bubble

The dynamics of an uncoated bubble in free space was first described by Lord Rayleigh [35] and was later refined by Plesset [31], Noltingk & Neppiras [29,30] and Poritsky [32] to account for surface tension and viscosity of the liquid. A popular version of the equation of motion describing the bubble dynamics

(often referred to as *the* Rayleigh-Plesset equation) is given by:

$$\rho\left(\ddot{R}R+\frac{3}{2}\dot{R}^2\right)= \left(P_0+\frac{2\sigma_w}{R_0}\right)\left(\frac{R_0}{R}\right)^{3\kappa}\left(1-\frac{3\kappa\dot{R}}{c}\right)-P_0-P_a(t)-4\nu\rho\frac{\dot{R}}{R}-\frac{2\sigma_w}{R}, \quad (7.1)$$

where $\rho$ is the liquid density, $\nu$ the kinematic viscosity of the liquid, $c$ the speed of sound in the liquid, $\sigma_w$ the surface tension of the gas-liquid system and $\kappa$ the polytropic exponent of the gas inside the bubble. $P_0$ is the ambient pressure and $P_a(t)$ the applied acoustic pressure. $R_0$ is the initial bubble radius, $R$ represents the time-dependent radius of the bubble, while $\dot{R}$ and $\ddot{R}$ represent the velocity and the acceleration of the bubble wall, respectively. The bubble is assumed to be surrounded by an infinite medium and it remains spherical during oscillations. The bubble radius is small compared to the acoustic wavelength. The gas content of the bubble is constant. Damping of the bubble dynamics is governed by viscous damping of the surrounding liquid and by acoustic radiation damping, through sound radiated away from the bubble [11, 12, 15, 17, 20, 21, 34, 37]. For the sake of simplicity thermal damping is not included here. Finally, the density of the liquid is large compared to the gas density.

### 7.2.1 Linearized equations

We often use the linearized equations to describe the bubble dynamics at low driving pressures. For small amplitudes of oscillation the time-dependent radius $R$ can be written as $R = R_0\,(1 + x\,(t))$. Through a linearization of the Rayleigh-Plesset equation around the initial radius $R_0$ we obtain:

$$\ddot{x}+\omega_0\delta\dot{x}+\omega_0^2x=F(t), \quad (7.2)$$

with $x$ its relative radial excursion, $f_0 = \omega_0/2\pi$ the eigenfrequency of the system and $\delta$ the dimensionless damping coefficient. $F(t) = F_0 sin(\omega t)$ is the acoustic forcing term. The eigenfrequency of the system follows from (7.1) and (7.2).

$$f_0=\frac{1}{2\pi}\sqrt{\frac{1}{\rho R_0^2}\left(3\kappa P_0+(3\kappa-1)\,\frac{2\sigma_w}{R_0}\right)}. \quad (7.3)$$

The total damping coefficient ($\delta$) is given by the sum of the individual damping coefficients. The contribution from the sound radiated by the bubble ($\delta_{rad}$) is:

$$\delta_{rad}=\frac{\dfrac{3\kappa}{\rho cR_0}\left(P_0+\dfrac{2\sigma_w}{R_0}\right)}{\omega_0}\approx\frac{\omega_0R_0}{c}, \quad (7.4)$$

and the viscous contribution ($\delta_{vis}$) is:

$$\delta_{vis} = \frac{4\nu}{\omega_0 R_0^2}. \tag{7.5}$$

The resonance frequency of the system is then obtained from:

$$f_{res} = f_0 \sqrt{1 - \frac{\delta^2}{2}}. \tag{7.6}$$

For a free gas bubble the damping coefficient is negligible. The surface tension is negligible in the mm size range and the resonance frequency is given by the Minnaert frequency [28]:

$$f_{res} \approx f_0 = \frac{1}{2\pi} \sqrt{\frac{3\kappa P_0}{\rho R_0^2}}. \tag{7.7}$$

For an air bubble in water we then recover the common rule of thumb for the bubble resonance $f_0 R_0 \approx 3$ mm kHz. It should be noted that for bubbles with a radius $<$ 10 μm the surface tension cannot be neglected.

Assuming a steady-state response ($t \to \infty$), substitution into equation 7.2 gives the absolute relative amplitude of oscillation:

$$|x_0| = \frac{F_0}{\sqrt{\left(\omega_0^2 - \omega^2\right)^2 + \left(\delta \omega \omega_0\right)^2}}. \tag{7.8}$$

For small damping, as in the case of a free gas bubble, the amplitude of oscillations of a bubble driven at a frequency well below its resonance frequency is inversely proportional to the effective 'mass' and the eigenfrequency squared of the system (stiffness-controlled). Well above the resonance frequency the amplitude of oscillation is inversely proportional to the effective 'mass' of the system (inertia-driven). Close to resonance the amplitude of oscillation is inversely proportional to the damping coefficient, the eigenfrequency squared and the effective 'mass' of the system [25].

## 7.3 Coated bubbles

Ultrasound contrast agents are encapsulated with a phospholipid, protein, palmitic acid or polymer coating. The coating shields the water from the gas, reducing the surface tension to prevent the bubbles from dissolution. Several Rayleigh-Plesset type models have been derived for coated bubbles. Church [6] derived a theoretical model for a coated bubble assuming that the gas core is separated from the liquid by a layer of an incompressible, solid elastic material. The shell has a finite thickness and the shell elasticity and

the shell viscosity depend on the rigidity of the shell and the thickness of the shell. Commercial 1st generation Albunex (Mallinckrodt) microbubbles have an albumin shell and remain stable for an extended period of time at atmospheric pressure. Therefore, in Church's model it is assumed that the elastic shell counteracts the capillary pressure ($P_{g0} = P_0$) which stabilizes the bubble against dissolution.

The second generation contrast agents have a more flexible phospholipid shell. The commercially available contrast agents Sonovue® (Bracco), Definity (Lantheus Medical Imaging) and Sonazoid (GE) consist of a monolayer of phospholipids with a thickness of a few nanometers. Various models account for a (phospholipid) coating by assuming a viscoelastic thin shell, see for example De Jong et al. [7], Hoff et al. [18] and more recently Sarkar et al. [36]. The Rayleigh-Plesset type models account for the shell by an effective surface tension ($\sigma(R)$) and the addition of a friction term ($S_{fric}$) due to the shell elasticity and viscosity, respectively.

$$\rho\left(\ddot{R}R + \frac{3}{2}\dot{R}^2\right) = P_{g0}\left(\frac{R_0}{R}\right)^{3\kappa}\left(1 - \frac{3\kappa\dot{R}}{c}\right) - P_0 - P_a(t) - 4\nu\rho\frac{\dot{R}}{R} - \frac{2\sigma(R)}{R} - 4S_{fric}\frac{\dot{R}}{R^2}. \tag{7.9}$$

Hoff et al. [18] modified Church's model to account for the thin shell by reducing the equation of Church to a form similar to that of equation 7.9. The effective surface tension and the shell viscosity in the various models are given in Table 7.1. The effective surface tension changes as a function of the bubble radius, see Figure 7.3 for a plot for the various shell models. The parameters are chosen to be comparable in the models ($S_p = 2E_s = 6G_s d_{sh0} = 1.1$ N/m) for the shell elasticity and ($S_f = 16\pi\kappa_s = 48\pi\mu_s d_{sh0} = 2.7 \cdot 10^{-7}$ kg/s) for the shell viscosity, as reported by Gorce et al. [16]. In this regime, the slope of the effective surface tension as a function of the bubble radius is similar for the

**Table 7.1.** Values for the initial gas pressure in the bubble ($P_{g0}$), the effective surface tension $\sigma(R)$ and the shell viscosity $S_{fric}$ for three elastic shell models. For comparison the values for an uncoated bubble (Rayleigh-Plesset) are also given

| *Model* | $P_{g0}\,[\mathrm{N/m^2}]$ | $\sigma(R)\,[\mathrm{N/m}]$ | $S_{fric}\,[\mathrm{kg/s}]$ |
|---|---|---|---|
| Rayleigh-Plesset | $P_0 + \frac{2\sigma_w}{R_0}$ | $\sigma_w$ | – |
| Church [6], Hoff et al. [18] | $P_0$ | $6G_s d_{sh0}\frac{R_0^2}{R^2}\left(1 - \frac{R_0}{R}\right)$ | $3\mu_s d_{sh0}\frac{R_0^2}{R^2}$ |
| De Jong et al. [7] | $P_0 + \frac{2\sigma_w}{R_0}$ | $\sigma_w + S_p\left(\frac{R}{R_0} - 1\right)$ | $\frac{S_f}{16\pi}$ |
| Sarkar et al. [36] | $P_0$ | $\sigma(R_0) + E_S\left(\frac{R^2}{R_E^2} - 1\right)$ | $\kappa_s$ |

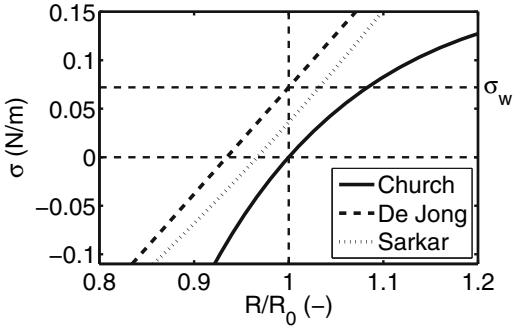


**Fig. 7.3.** The effective surface tension as a function of the bubble radius ($R_0 = 2\,\mu$m) for the different models accounting for a purely elastic shell

models by De Jong et al. [7] and Sarkar et al. [36]. The main difference between the models is found for the effective surface tension at the initial bubble radius ($\sigma(R_0)$). It equals $\sigma_w$ for the model by De Jong et al. [7] and it varies for the model by Sarkar et al. [36]. In this example we choose $\sigma(R_0) = 0.036$ N/m for the model of Sarkar et al. [36]. The model of Church [6], modified by Hoff et al. [18] for a thin shell, has a lower initial effective surface tension, $\sigma(R_0) = 0$ N/m, and has a different slope. Note that the effective surface tension in these models is not bound and the effective surface tension can become negative and larger than $\sigma_w$.

Marmottant et al. [26] introduced a model which seems to be more applicable for high amplitude oscillations. The model accounts for an elastic shell and also for buckling and rupture of the shell. When the shell is elastic, compression of the bubble increases the phospholipid concentration. Therefore, in the elastic regime the effective surface tension decrease is a linear function of the area under compression. Further compression leads to such high phospholipid concentrations that the shell tends to buckle and the effective surface tension vanishes. On the other hand, expansion decreases the phospholipid concentration and leads to rupture. It is assumed that the effective surface tension will relax to $\sigma_w$. The effective surface tension using equation 7.9 for the three regimes is given by:

$$\sigma(R) = \begin{cases} 0 & \text{if} \quad R \leq R_{buckling} \\ \chi\left(\dfrac{R^2}{R_{buckling}^2} - 1\right) & \text{if} \quad R_{buckling} \leq R \leq R_{breakup} \\ \sigma_w & \text{if ruptured and } R \geq R_{breakup} \end{cases}, \tag{7.10}$$

with $\chi$ the shell elasticity and $R_{buckling}$ and $R_{breakup}$ the buckling and breakup radius, respectively. The effective surface tension as a function of the relative radius for the Marmottant model is shown in Figure 7.4. The shell of a UCA microbubble consists of a monolayer of phospholipids. The initial surface ten-

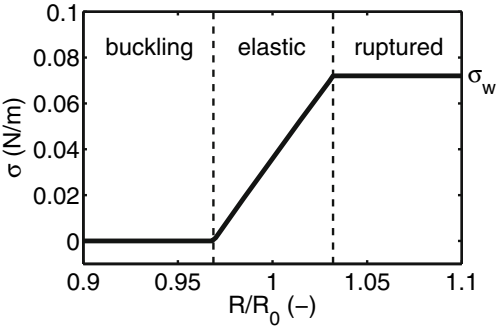


**Fig. 7.4.** The effective surface tension as a function of the bubble radius ($R_0 = 2\,\mu$m) for the model of Marmottant et al. (2005) including an elastic regime and buckling and rupture of the shell

sion is chosen to be $\sigma(R_0) = 0.036$ N/m similar to the example of the Sarkar model. The choice of $\sigma(R_0)$ in combination with the value for the shell elasticity $\chi = S_p/2 = 0.55$ N/m results in $R_{buckling} = 0.97\ R_0$ and $R_{breakup} = 1.03\ R_0$. In this example the bubble is assumed to rupture when the surface tension reaches $\sigma_w$. The shell viscosity in equation 7.9 is given by $S_{fric} = \kappa_s$. As will be shown in the following paragraph, the elasticity of the shell increases the eigenfrequency of the bubble while the shell viscosity increases the total damping of the system.

### 7.3.1 Linearized equations

The bubble resonance frequency and its corresponding damping coefficient are derived in a similar way as in section 7.2.1. For the model of De Jong et al. [7] the eigenfrequency and the total damping ($\delta_{tot} = \delta_{rad} + \delta_{vis} + \delta_{shell}$) are given by:

$$f_0 = \frac{1}{2\pi}\sqrt{\frac{1}{\rho R_0^2}\left(3\kappa P_0 + (3\kappa - 1)\,\frac{2\sigma_w}{R_0} + \frac{2S_p}{R_0}\right)} \tag{7.11}$$

$$\delta_{tot} = \frac{\dfrac{3\kappa}{\rho c R_0}\left(P_0 + \dfrac{2\sigma_w}{R_0}\right)}{\omega_0} + \frac{4\nu}{\omega_0 R_0^2} + \frac{S_f}{4\pi\rho R_0^3 \omega_0}. \tag{7.12}$$

The eigenfrequency of a coated bubble has two contributions: one part that is similar to the eigenfrequency of an uncoated bubble and an elastic shell contribution. The shell viscosity $S_f$ increases the damping for a coated bubble. Figure 7.5 shows the eigenfrequency and resonance frequency for an uncoated and coated bubble. The resonance frequency and the eigenfrequency of the uncoated bubble agree to within graphical resolution. The eigenfrequency of a coated bubble in comparison to an uncoated microbubble is higher due to

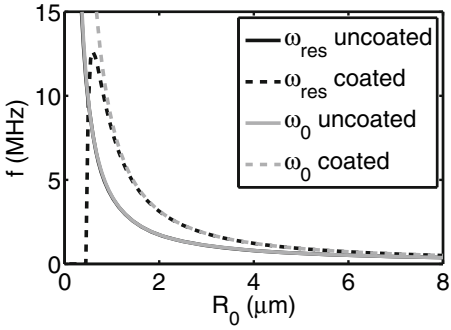


**Fig. 7.5.** The resonance frequency as a function of the initial bubble radius ($R_0$) for an uncoated (dotted black line) and coated microbubble (dashed black line). For comparison the eigenfrequency is plotted (grey). The resonance frequency and the eigenfrequency of the uncoated bubble agree to within graphical resolution

the shell elasticity. The damping has a negligible influence on the resonance frequency for an uncoated bubble and for coated bubbles with $R_0 > 1$ μm. Figure 7.6 shows the resonance curve of an uncoated and coated microbubble with a resting radius of 2 μm. The amplitude of oscillation and the resonance frequency are normalized to the maximum amplitude of oscillation and the resonance frequency of the uncoated bubble, respectively. Both the damping and eigenfrequency increase for a coated microbubble, while the effective 'mass' stays the same. The amplitude of oscillation at resonance is therefore lower when the bubble has a shell, see Figure 7.6. Below resonance, neglecting the influence of the damping, the system is stiffness driven. The shell increases the stiffness of the system and the amplitude of oscillation below resonance is therefore lower for a coated microbubble. Far above resonance the amplitude

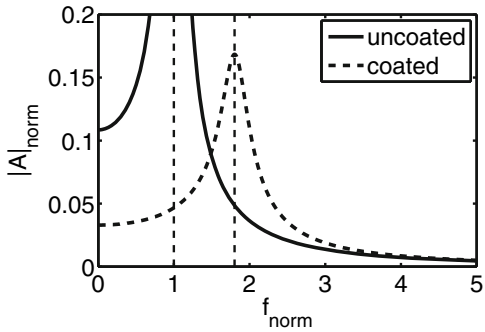


**Fig. 7.6.** The amplitude of oscillation for an uncoated and coated bubble with $R_0 = 2$ μm, normalized with the maximum amplitude of oscillation of the uncoated microbubble. The driving frequency is normalized to the resonance frequency of the uncoated microbubble

of oscillation is inversely proportional to the effective 'mass' of the system. Consequently above resonance the amplitude of oscillation does not depend on the shell properties.

### 7.3.2 Optical and acoustical characterization

The theoretical models are validated through experiments on single bubbles. Acoustical and optical experiments reveal the response of UCA microbubbles and both have there own particular advantages and disadvantages. In acoustical experiments, the scattered pressure or pressure-time $P$-$t$ curve is recorded. Acoustic characterization is relatively inexpensive and has the advantage of a high sampling rate using long pulse sequences. The scattered pressure of a single bubble however is limited (order 1 Pa) and close to the noise level of our detection system. The transducer focus is in the order of the acoustic wavelength and a bubble must be isolated in the in vitro setup. In optical experiments high-speed cameras are used to record the radial response or radius-time $R$-$t$ curve of single bubbles. Such a camera should be able to temporally resolve the dynamics of the microbubbles which is driven at MHz frequencies. The required framerates makes the construction of such a camera expensive. The recording time is limited by the number of frames. Optical characterization of single microbubbles is relatively easy. The Brandaris 128 camera, see Figure 7.2, was especially designed for this purpose [5]. The camera uses a fast rotating mirror (max 20,000 rps) to sweep the image across 128 highly sensitive CCDs. At maximum speed an interframe time of 40 ns, which corresponds to a framerate of 25 Mfps is obtained. Figure 7.7 shows a sequence of 25 frames recorded with the Brandaris 128 camera at a framerate of 13.5 Mfps. The applied acoustic pulse has a frequency of 2.7 MHz and a pressure of 30 kPa. The accompanying $R$-$t$ curve of the microbubble from the Brandaris movie is shown in Figure 7.8. The maximum amplitude of oscillation is 200 nm corresponding to a relative amplitude of 10%.

The first fitting of shell parameters for SonoVue® were performed acoustically on a microbubble suspension [16]. Recently, optical $R$-$t$ curves of single UCA microbubbles (SonoVue®) were recorded and fitted, to an elastic shell model (Hoff's model), by Chetty et al. [4]. In Chetty et al. [4] the shell thickness and shell viscosity was fixed and it was found that the shell elasticity increases with increasing bubble radius. The experiments were performed with a single applied frequency (0.5 MHz) and pressure (40-80 kPa). No experiments were performed to test the validity of the shell parameters for the same bubble at different ultrasound frequencies and pressures. Van der Meer et al. [38] insonified single UCA microbubbles (BR-14) consecutively with 11 ultrasound pulses, increasing the frequency for each pulse, near resonance. A resonance curve was then obtained by plotting the amplitude of oscillation as a function of the applied frequency. A fit of the resonance curve to the linearized shell model of Marmottant et al. [26] then resulted in the shell elasticity and shell viscosity. In contrast to Chetty et al. [4], Van der Meer

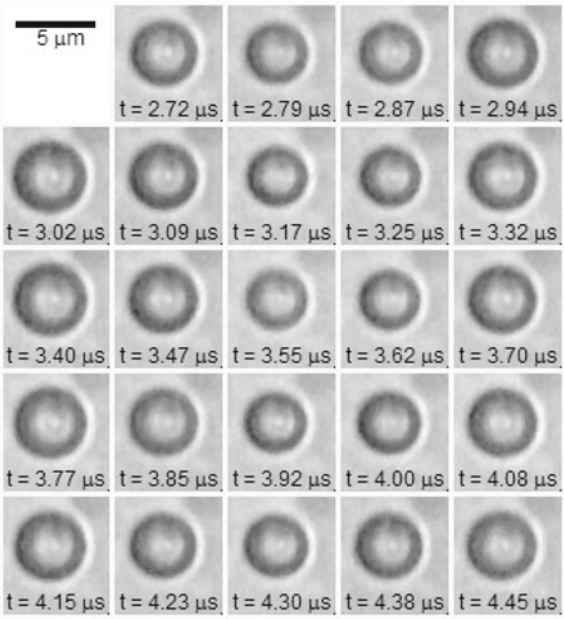


**Fig. 7.7.** Sequence of 24 frames of a 2.2 µm radius bubble recorded with the Brandaris 128 camera at a framerate of 13.5 Mfps

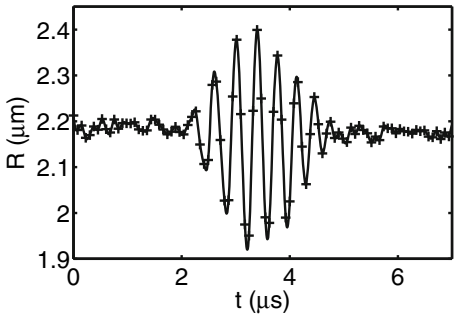


**Fig. 7.8.** The R-t curve of the same bubble as in Figure 7.7. The bubble is insonified with an ultrasound pulse with a frequency of 2.7 MHz and an acoustic pressure of 30 kPa

et al. [38] found that the shell elasticity was nearly constant while the shell viscosity decreases with decreasing dilatation rate $\left(\dot{R}/R\right)$. One should note that all the above experiments were performed at or in close proximity to a (capillary) wall. In the following section we will discuss the influence of a rigid wall on bubble dynamics.

De Jong et al. [8] reported on an observation of coated microbubbles at low applied acoustic pressures, where the bubbles compress, but hardly expand.

This highly non-linear effect, referred to as compression-only behavior, occurs for 40% of the bubbles even at pressures as low as 50 kPa. Remarkably all bubbles with an initial radius less than 2 μm show compression only behavior at a frequency of 1 MHz. Compression only behavior is not observed for uncoated bubbles and cannot be described by a model accounting for purely an elastic shell. Actually, the purely elastic shell models predict even a decrease of the non-linear behavior of the coated microbubbles as compared to the dynamics of an uncoated microbubble. The model of Marmottant et al. [26] accounting for an elastic shell and for buckling and rupture of the shell predicts compression-only behavior. As stated by Marmottant et al. [26] the compression modulus in the elastic state is much higher than in the buckled or ruptured state. For a bubble where the resting radius is the buckling radius it is much harder to expand than to compress and results in compression only behavior of the bubble [26].

Emmer et al. [10] showed an oscillation threshold for coated microbubbles with a radius smaller than 2.5 μm at a driving frequency of 1.7 MHz. Below a certain pressure (30–120 kPa) the bubbles hardly oscillate while above this threshold the amplitude of oscillation increases linear with the applied acoustic pressure. This non-linear effect occurs at low acoustic pressures and is not yet fully understood. The non-linear behavior of the UCA microbubbles can be exploited to improve present contrast enhanced imaging techniques.

## 7.4 Bubble dynamics near a rigid wall

In this section we discuss the influence of a rigid wall on the bubble dynamics. We start with the simplest approach, the so-called method of images, to simulate the influence of a wall. We also study the system experimentally by recording the radial bubble dynamics at the wall and in free space, away from the wall.

### 7.4.1 Method of images

In the literature, several extensions to the bubble dynamics equations have been made to account for the presence of a rigid wall. All the models described here are based on the method of images depicted in Figure 7.9. If the wall is rigid, the specific acoustic impedance $Z = \rho\, c$ is infinite, and no energy crosses the wall. To describe the acoustic (or equivalently the fluid-mechanical field) the wall is replaced by an identical image bubble oscillating in-phase with the real bubble and positioned at the mirrored image point. The real bubble dynamics is influenced by the pressure emitted by the image bubble. The dynamics of a coated bubble near a rigid wall is therefore described by a Rayleigh-Plesset type equation including the radiated pressure of the image

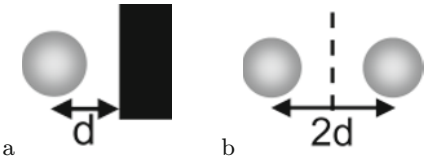


**Fig. 7.9.** The method of images. In (**a**) the actual situation, where the bubble is located at a distance $d$ from the rigid wall, (**b**) shows the method of images in which the wall is replaced by an image bubble

bubble:

$$\rho\left(\ddot{R}R+\frac{3}{2}\dot{R}^2\right)=P_{g0}\left(\frac{R_0}{R}\right)^{3\kappa}\left(1-\frac{3\kappa\dot{R}}{c}\right)-P_0 \\ -P_a(t)-4\nu\rho\frac{\dot{R}}{R}-4S_{fric}\frac{\dot{R}}{R^2}-\frac{2\sigma\left(R\right)}{R}-\rho\frac{\partial}{\partial t}\left(\frac{\dot{R}R^2}{2d}\right), \tag{7.13}$$

where $d$ represents the distance between the bubble and the wall. For a bubble positioned directly at the wall, such as bubbles floating up against the capillary wall, the distance $d$ is simply given by the bubble radius $R\left(t\right)$. In this case the bubble dynamics equation becomes:

$$\rho\left(\frac{3}{2}\ddot{R}R+2\dot{R}^2\right)=P_{g0}\left(\frac{R_0}{R}\right)^{3\kappa}\left(1-\frac{3\kappa\dot{R}}{c}\right)-P_0 \\ -P_a(t)-4\nu\rho\frac{\dot{R}}{R}-4S_{fric}\frac{\dot{R}}{R^2}-\frac{2\sigma\left(R\right)}{R}. \tag{7.14}$$

Note that all assumptions made previously for the Rayleigh-Plesset equation for an uncoated microbubble remain valid. Therefore the bubble must remain spherical, which may not be strictly true in the experimental situation. For example we know that bubbles deform close to the wall at pressures of 140 kPa [39].

### 7.4.2 Linearized equations

The rigid wall increases the effective 'mass' of the bubble 3/2 times (increased prefactor of the inertial term) resulting in a decrease of the eigenfrequency and damping. For an (un)coated bubble at a wall, the eigenfrequency and damping are derived in a similar way as in section 7.2.1. The eigenfrequency and damping for an uncoated bubble reduce to:

$$f_0^{wall}=\sqrt{\frac{2}{3}}f_0^{free}\approx 0.8f_0^{free} \\ \delta^{wall}=\sqrt{\frac{2}{3}}\delta^{free}\approx 0.8\delta^{free}. \tag{7.15}$$

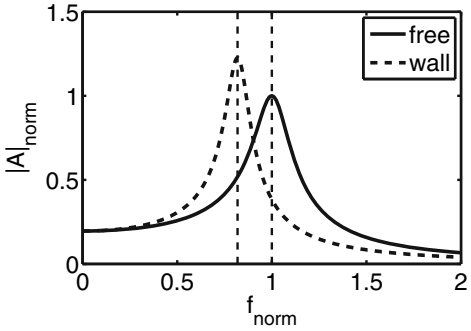


**Fig. 7.10.** Resonance curves for an uncoated bubble with a initial radius of 2 μm in free space (solid), at a rigid wall. The frequency and the amplitude are normalized with the resonance frequency and amplitude of oscillation at resonance in the free case

Figure 7.10 shows the resonance curve of a coated bubble in free space (solid) and at the wall (dashed). The amplitude of oscillation and the applied frequency are normalized to that of the bubble in free space. The amplitude of oscillation at resonance is $\sqrt{3/2}$ larger for a bubble at a wall than for a free bubble, see Figure 7.10. Below the resonance frequency the amplitude of oscillations remains unchanged (stiffness-controlled) while above resonance the amplitude of oscillation is 1.5 times smaller for a bubble at a wall because of the increased effective 'mass' of the system.

### 7.4.3 Observations

Bubbles injected in an in vitro setup (e.g. capillary or flow cell) float up due to buoyancy until they reach the top wall. Due to the limited focal depth of the microscope objective the rising bubbles are difficult to capture in free space. The radial bubble dynamics is therefore traditionally captured with the bubbles positioned against the top wall of the capillary. In order to study the influence of a wall on the bubble dynamics, the radial bubble response should also be recorded in free space. To investigate the bubbles in free space we trap the microbubbles and control their position in 3D space.

The pioneering work on particle trapping was that of Ashkin [1], who showed the first optical trap for high-index particles $\left(n = n_{particle}/\, n_{medium} > 1\right)$. Optical trapping has undergone rapid development, attracting special attention from the life science discipline, as nanoparticles, cells, viruses and bacteria can be micromanipulated and controlled. A high-index particle is trapped in the intensity maximum of the laser beam focus. The optical gradient force is directed towards the intensity maximum, while the scattering force, away from the intensity maximum cancels out. Low-index particles, such as the microbubbles studied here $\left(n = n_{particle}/n_{medium} < 1\right)$, are repelled by both the scattering force and the gradient force. They can, however, be

trapped in the intensity minimum in the center of a donut-shaped Laguerre-Gaussian (LG) laser beam [13]. LG beams are obtained by modulating the phase of a Gaussian beam, using diffractive optical elements (DOEs).

To investigate the influence of a wall on the dynamics of coated microbubbles, Garbin et al. [14] combined an optical tweezers setup with the ultra-high speed Brandaris 128 camera. This enabled the micromanipulation of single UCA microbubbles in 3D space, thereby temporally resolving bubble dynamics, which as a result allowed for a detailed investigation of the influence of the flow cell wall. Figure 7.11 shows the *R-t* curves of a single bubble with a radius of 2.5 μm insonified with a frequency of 2.25 MHz and a pressure of 200 kPa. The top figure shows the *R-t* curve of the bubble at the flow cell wall, while the middle figure shows the *R-t* curve of the very same bubble positioned 50 μm away from the wall in free space. The bottom figure shows the bubble response back at the wall and the amplitude of oscillation is similar as in the first experiment where the bubble was also located at the wall. Garbin et al. [14] reported a decrease in the amplitude of oscillations at the flow cell wall by over 50%.

The following three possible explanations for the decrease in amplitude at the wall were discussed in Garbin et al. [14]. First, a change in the resonance frequency caused by the presence of the wall. This explanation is consistent with the models described here, that show a decrease of the resonance frequency by 20%. A viscous boundary layer formed near the wall inducing shear stresses and additional dissipation was suggested as a second mechanism to explain the observed behavior. Up to now simulations describing the boundary layer approach have failed to predict the decrease of the amplitude of oscilla-

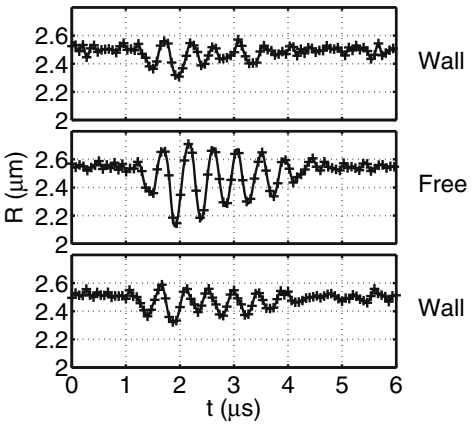


**Fig. 7.11.** R-t curves for a single microbubble with a radius of 2.5 μm. The applied ultrasound has a frequency of 2.25 MHz and a pressure of 200 kPa. The microbubble is insonified at the wall (top), in free space 50 μm away from the wall (middle) and again at the wall (bottom)

tions near the wall. A third explanation that was given in Garbin et al. [14] were non-spherical oscillations caused by the non-symmetrical interaction of the oscillating bubble with the wall. In the setup by Garbin et al. [14] non-spherical oscillations could not be observed due to the optical configuration employed. The optical axis was perpendicular to the flow cell wall, i.e. it was always observed in top-view. Voss et al. [39] showed, with a setup allowing both, a side-view (optical axis parallel to the wall) and a top-view that the oscillations of UCA microbubbles may appear spherical in top-view and can be quite asymmetric in side-view.

Until now dissipation caused by translational oscillations due to secondary Bjerknes force was not considered. A microbubble in an incident acoustic wave will experience an acoustic radiation force. The force $\mathbf{F}$ depends on the volume of the bubble $V$ and the acoustic pressure gradient $\boldsymbol{\nabla} P$:

$$\mathbf{F} = -V \boldsymbol{\nabla} P. \tag{7.16}$$

The force is called the (primary) Bjerknes force [2] if it is caused by the incident acoustic wave. An oscillating microbubble radiates sound (pressure waves) and thereby induces an acoustic radiation force on its neighboring bubble, termed the secondary Bjerknes force. The Bjerknes force leads to an alternating attractive and repulsive translation. Bubbles oscillating in phase have a net attractive force while bubbles oscillating out of phase repel each other. Consequently, a microbubble near a rigid wall will experience a net attractive force towards the wall, as its image bubble oscillates in phase.

For the simulations described here the wall is considered as an infinitely thick rigid wall. No energy passes the wall and the ultrasound will be fully reflected at the wall. In our experiments the wall is acoustically transparent to allow ultrasound to enter the flow cell and to prevent unwanted reflections. For such a compliant wall the (complex) amplitude of the image bubble needs to be adapted to the wall properties and this will be the subject of a future study.

## 7.5 Conclusions

A phospholipid coating is accounted for by a thin viscoelastic layer. The shell elasticity increases the eigenfrequency while a shell viscosity increases the total damping and decreases the amplitude of oscillations of coated bubbles. Most models, valid for low amplitude oscillations, describe the shell as fully elastic [7,18,36] and predict a decrease in the linear and the non-linear behavior of coated microbubbles. Experiments show non-linear behavior for coated microbubbles at low applied acoustic pressure, for example, compression only behavior and thresholding behavior. The model of Marmottant et al. [26] including buckling and rupture of the shell is valid for high amplitude oscillations and predicts the observed compression only behavior.

With the method of images a decrease in the resonance frequency and an increase of the amplitude at resonance is predicted for uncoated and coated bubbles. These models do not include boundary layers and the oscillations are assumed to remain spherical at all times.

The change in the dynamics of UCA microbubbles near a wall Garbin et al. [14] is important for molecular imaging applications. The next step after understanding the influence of a phospholipid shell and a wall is to understand the influence of ligands on the coating, and targeting the wall. Optimization of pulse-echo techniques can be done when there is a full understanding of the complex systems.

**Acknowledgements**
We thank many of our collaborators on this subject for their great help: Benjamin Dollet, Marcia Emmer, Valeria Garbin, Todd Hay, Sascha Hilgenfeldt, Detlef Lohse, Philippe Marmottant, Sander van der Meer, Jeroen Sijl, and Timo Rozendal. We gratefully acknowledge the technical assistance of Wim van Alphen, Leo Bekkering, Martin Bos, Gert-Wim Bruggert, Jan Honkoop, Frits Mastik, Cees Pakvis, and Geert Springeling in constructing and improving our experimental setups. We acknowledge Bracco Research S.A. (Geneva) for providing BR-14 vials and for stimulating discussions. This work is financially supported by TAMIRUT, under project nr. NMP4-CT-2005-016382.

## References

1. Ashkin A (1986) Observation of a single-beam gradient force optical trap for dielectric particles. Optics Letters 11(5):288
2. Bjerknes V (1906) Fields of Force. Columbia University Press
3. Brock-Fisher G, Poland M and Rafter P (1996) Means for increasing sensitivity in non-linear ultrasound imaging systems US patent no 55775
4. Chetty K, Stride E, Sennoga C, Hajnal J and Eckersley R (2008) High-speed optical observations and simulation results of sonovue microbubbles at low-pressure insonation. IEEE Transactions on Ultrasonics, Ferroelectrics, and Frequency Control 55(6):1333–1342
5. Chin C, Lancee C, Borsboom J, Mastik F, Frijlink M, de Jong N, Versluis M and Lohse D (2003) Brandaris 128: A digital 25 million frames per second camera with 128 highly sensitive frames. Review of Scientific Instruments 74:5026–5034
6. Church C (1995) The effects of an elastic solid surface layer on the radial pulsations of gas bubbles. The Journal of the Acoustical Society of America 97(3):1510–1521
7. De Jong N, Cornet R and Lancee CT (1994) Higher harmonics of vibrating gas-filled microspheres. part one: simulations. Ultrasonics 32:447–453
8. De Jong N, Emmer M, Chin C, Bouakaz A, Mastik F, Lohse D and Versluis M (2007) "compression-only" behavior of a phosphorlipid-coated contrast bubbles. Ultrasound in Medicine and Biology 33(4)
9. Doinikov A (2001) Translational motion of two interacting bubbles in a strong acoustic field. Physical Review E 64(2):026,301

10. Emmer M, Wamel AV, Goertz D and Jong ND (2007) The onset of microbubble vibration. Ultrasound in Medicine and Biology 33(6):941–949
11. Flynn H (1975a) Cavitation dynamics. i. a mathematical formulation. The Journal of the Acoustical Society of America 57(6):1379–1396
12. Flynn H (1975b) Cavitation dynamics: Ii. free pulsations and models for cavitation bubbles. The Journal of the Acoustical Society of America 58(6):1160–1170
13. Gahagan K (1996) Optical vortex trapping of particles. Optics Letters 21(827):11
14. Garbin V, Cojoc D, Ferrari E, Fabrizio ED, Overvelde M, van der Meer S, de Jong N, Lohse D and Versluis M (2007) Changes in microbubble dynamics near a boundary revealed by combined optical micromanipulation and high-speed imaging. Applied Physics Letters 90:114,103
15. Gilmore F (1952) The growth or collapse of a spherical bubble in a viscous compressible liquid. Tech. rep., Hydrodynamics Laboratory, California Institute Technology, Pasadena, report 26–4
16. Gorce JM, Arditi M and Schneider M (2000) Influence of bubble size distribution on the echogenicity of ultrasound contrast agents. Investigative Radiology 35(11):661–671
17. Herring C (1941) Theory of the pulsations of the gas bubble produced by an underwater explosion. Tech. rep., OSRD report 236
18. Hoff L, Sontum P and Hovem J (2000) Oscillations of polymeric microbubbles: Effect of the encapsulating shell. The Journal of the Acoustical Society of America 107(4):2272–2280
19. Hope Simpson D, Ting CC and Burns P (1999) Pulse inversion doppler: a new method for detecting nonlinear echoes from microbubble contrast agents. IEEE Transactions on Ultrasonics, Ferroelectrics, and Frequency Control 46(2):372–382
20. Keller J and Kolodner I (1956) Damping of underwater explosion bubble oscillations. Journal of Applied Physics 27(10):1152–1161
21. Keller JB and Miksis M (1980) Bubble oscillations of large amplitude. The Journal of the Acoustical Society of America 68:628–633
22. Klibanov A (2002) Ultrasound Contrast Agents: Development of the Field and Current Status, Topics in Current Chemistry 222
23. Lankford M, Behm C, Yeh J, Klibanov A, Robinson P and Linder J (2006) Effect of microbubble ligation to cells on ultrasound signal enhancement: implications for targeted imaging. Investigative Radiology 41(10)
24. Lauterborn W (1976) Numerical investigation of nonlinear oscillations of gas bubbles in liquids. The Journal of the Acoustical Society of America 59(2):283–293
25. Leighton T (1994) The Acoustic Bubble. Academic Press Inc. San Diego
26. Marmottant P, van der Meer S, Emmer M, Versluis M, de Jong N, Hilgenfeldt S and Lohse D (2005) A model for large amplitude oscillations of coated bubbles accounting for buckling and rupture. The Journal of the Acoustical Society of America 118:3499–3505
27. Marmottant P, Versluis M, Jong ND, Hilgenfeldt S and Lohse D (2006) High-speed imaging of an ultrasound-driven bubble in contact with a wall: "narcissus" effect and resolved acoustic streaming. Experiments in Fluids 41(2):147–153
28. Minnaert M (1933) On musical air-bubbles and sounds of running water. Philosophical Magazine 16:235–248

29. Neppiras E and Noltingk B (1951) Cavitation produced by ultrasonics: Theoretical conditions for the onset of cavitation. Proceedings of the Physical Society Section B 64(12):1032–1038
30. Noltingk B and Neppiras E (1950) Cavitation produced by ultrasonics. Proceedings of the Physical Society Section B 63(9):674–685
31. Plesset M (1949) The dynamics of cavitation bubbles. Journal of Applied Mechanics 16:277–282
32. Poritsky H (1952) The collapse or growth of a spherical bubble or cavity in a viscous fluid. Proceedings of the first US National Congress on Applied Mechanics pp 813–821
33. Prosperetti A (1975) Nonlinear oscillations of gas bubbles in liquids. transient solutions and the connection between subharmonic signal and cavitation. The Journal of the Acoustical Society of America 57(4):810–821
34. Prosperetti A, Crum L and Commander K (1988) Nonlinear bubble dynamics. The Journal of the Acoustical Society of America 83(2):502–514
35. Rayleigh L (1917) On the pressure developed in a liquid during the collapse of a spherical cavity. Philosophical Magazine 34:94–98
36. Sarkar K, Shi W, Chatterjee D and Forsberg F (2005) Characterization of ultrasound contrast microbubbles using in vitro experiments and viscous and viscoelastic interface models for encapsulation. The Journal of the Acoustical Society of America 118(1):539–550
37. Trilling L (1952) The collapse and rebound of a gas bubble. Journal of Applied Physics 23(1):14–17
38. Van der Meer S, Dollet B, Chin CT, Bouakaz A, Voormolen M, de Jong N, Versluis M and Lohse D (2007) Microbubble spectroscopy of ultrasound contrast agents. The Journal of the Acoustical Society of America 120:3327–3327
39. Vos H, Dollet B, Bosch J, Versluis M and de Jong N (2008) Nonspherical vibrations of microbubbles in contact with a wall – a pilot study at low mechanical index. Ultrasound in Medicine and Biology 34(4):685–688
40. Zhao S, Ferrara K and Dayton P (2005) Asymmetric oscillation of adherent targeted ultrasound contrast agents. Applied Physics Letters 87(13)
41. Zhao S, Kruse D, Ferrara K and Dayton P (2006) Acoustic response from adherent targeted contrast agents. The Journal of the Acoustical Society of America 120(6):EL63–EL69